Cluster formation of network-modifier cations in cesium silicate glasses

Daniel Jardón-Álvarez,[1] Kevin J. Sanders,[2] Pyae Phyo,[3] Jay H. Baltisberger,[3] and Philip J. Grandinetti[1]
[1]*Department of Chemistry, Ohio State University, 100 West 18th Avenue, Columbus, Ohio 43210, USA*
[2]*Institut des Sciences Analytiques (CNRS UMR 5280, ENS de Lyon, UCB Lyon 1), Université de Lyon, 5 Rue de la Doua, 69100 Villeurbanne, France*
[3]*Division of Natural Science, Mathematics, and Nursing, Berea College, Berea, Kentucky 40403, USA*

(Received 29 December 2017; accepted 13 February 2018; published online 2 March 2018)

Natural abundance ^{29}Si two-dimensional magic-angle flipping (2D MAF) NMR spectra were measured in a series of ten cesium silicate glass compositions $x\mathrm{Cs_2O}\cdot(1-x)\mathrm{SiO_2}$, where x is 0.067, 0.113, 0.175, 0.179, 0.218, 0.234, 0.263, 0.298, 0.31, and 0.36. The Q^3 shielding anisotropy decreases with increasing Cs content—interpreted as an increase in the non-bridging oxygen (NBO) bond length from increasing Cs coordination (clustering) around the NBO. The ^{29}Si 2D MAF spectra for four glass compositions $x = 0.218$, 0.234, 0.263, 0.298 exhibit a second co-existing and distinctly smaller shielding anisotropy corresponding to a significantly longer Si–NBO length arising from a higher degree of Cs clustering around the NBO. This second Q^3 site appears at a Cs_2O mole fraction close to the critical mole fraction of $x = 0.24$ associated with the percolation threshold of non-bridging oxygen in random close packing of oxygen, thus suggesting that the longer Si–NBO length is associated with an infinite size spanning cluster while the sites with larger anisotropies are associated with shorter Si–NBO lengths and belong to finite size clusters. The equilibrium constant of the Q^3 disproportionation reaction was determined as $k_3 = 0.005$, indicating a Q^n anionic species distribution close to a binary model as expected for a low field strength modifier such as cesium. It is also found that evolution of the isotropic Q^4 and line shapes with increasing Cs content are consistent with a random connectivity model between Q^n of differing number of bridging oxygen, n. *Published by AIP Publishing.* https://doi.org/10.1063/1.5020986

I. INTRODUCTION

The introduction of non-network forming cations, also known as network-modifying cations, into silica, depolymerizes the silicate network by breaking bridging oxygen (BO) linkages and introduces non-bridging oxygen (NBO) linked to one silicon. This depolymerization results in marked changes in physical properties,[1–8] such as the glass transition temperature, viscosity, mechanical properties, and ionic (modifier cation) transport. While prediction of these properties rely heavily on various proposed structural models for the distribution of modifier cations,[9,10] obtaining detailed experimental evidence on the full extent of NBO and modifier cation cluster formation, size distributions, and degree of structural order at various length scales has been elusive.

In Zachariasen's seminal paper on glass structure,[11] he suggests that modifier cations fill holes in a three-dimensional framework of oxygen that "must be statistically distributed." In the 1938 paper of Warren and Biscoe on the continuous random network (CRN) structural model[12] for alkali and alkaline earth silicate glasses, they further propose that modifier cations—coordinated to NBO—in highly miscible glass compositions are expected to be uniformly distributed throughout the glass and be widely separated as they take part in the formation of the random silicon-oxygen network. The evolution of such a "random" or "statistical" distribution of modifier cations with increasing modifier content can be inferred through percolation theory.[13,14] In this context, percolation theory describes how randomly adding particle A (such as a NBO) to a network of particle B (such as a BO) leads to a well-defined critical threshold concentration, p_c, at which the dilute species will form clusters large enough to percolate through the entire network. Thus, the CRN model of statistically distributed modifier cations would naturally lead to the clustering of modifier cations and eventually percolation channels through which modifier cations are thought to move.[14,15] The critical concentration at which the percolation threshold occurs depends only on the geometry of the network. In the application of continuum percolation theory to glass structure, Scher and Zallen[14,16,17] made an important discovery in 1970 that the critical occupied volume fraction, defined as $\phi_c = fp_c$, where f is the filling factor of a lattice when sites are occupied by spheres, constitutes an approximate dimensional invariant for the threshold in site-percolation processes. For a network of randomly packed spheres, the percolation threshold is reached at a critical volumetric fraction of $\phi_c = 0.16$, which in a randomly close packed system[14] represents a critical concentration of sites $p_c^{site} = 0.27$. Dramatic changes in macroscopic properties in binary silicate glasses occurring at a modifier cation mole fraction near this critical concentration have been reported: Liang *et al.*[18] and Sen and Mukerji[19] report a strong increase in the diffusivity of silicate melts above a mole fraction of 25% and, similarly, Otto

and Milberg[20,21] found that the linear decrease in the activation energy for electrical conductivity in Cs and other binary alkali silicate glasses as a function of mole fraction undergoes a sharp break in the slope at 25%. Given the consistency of these macroscopic properties with percolation theory, one has to ask if microscopic evidence of an evolving structural distribution of modifier cations consistent with percolation theory also exists. Unfortunately, there are no definitive experimental probes of such intermediate to long-range modifier clustering.

Evidence of short-range modifier clustering around oxygen, however, is readily found in various experimental techniques. In isotope substitution neutron scattering experiments, Gaskell *et al.*[22] found strong evidence of short-range modifier clustering at the microscopic level in a $CaSiO_3$ glass. Oxygen-17 NMR isotropic line shape measurements of mixed alkali and alkaline earth silicates glasses of varying modifier compositions[23–27] were not only consistent with short-range clustering of modifiers around the NBO but also revealed strong deviations away from random mixing of modifiers with increasing differences in modifier cation potential.

In silicate networks, there are five types of SiO_4 tetrahedra, each characterized by their connectivity, i.e., the number of oxygens that are corner-linked to other tetrahedra. These are denoted by the notation Q^n, where n (~0–4) represents the number of bridging oxygen per tetrahedron. In two-dimensional (2D) NMR correlation experiments on ^{29}Si-enriched sodium silicate glasses, Jäger *et al.*[28] observed cross peaks (connectivities) between Q^n ($n < 4$)—i.e., direct evidence of a "cluster" of two Q^3 sites—and supporting evidence for short-range modifier clustering. Sadly, these 2D cross peaks are strongly overlapping in silicate glasses, difficult to assign, and nearly impossible to quantify.

Eckert and co-workers[29–34] used NMR measurements of ^{23}Na, ^{6}Li, and ^{7}Li nuclear dipolar couplings between modifier cations to distinguish between a uniform and a statistical spatial distribution. In both lithium and sodium borate glasses, the variation in the mean dipolar coupling was found to be consistent with a statistical distribution of modifiers at low modifier content.[33] In sodium and lithium silicate glasses, however, they observe stronger dipolar couplings than can be expected for either the uniform or statistical distribution of modifiers at low modifier content, concluding that these glasses possess a high degree of intermediate-range modifier clustering. Unfortunately, high liquidus temperatures and metastable immiscibilities out to 33 mol. % Li and out to 20 mol. % Na in these particular alkali silicate compositions make them prone to phase separation. No such measurements have been performed in alkali silicate compositions where there is little liquid-liquid immiscibility, such as K, Rb, or Cs silicates.[1]

In ^{29}Si Magic-Angle Flipping (MAF) measurements of alkali and alkaline earth silicate glasses,[35–38] we noted a systematic decrease in the ^{29}Si shielding anisotropy with increasing modifier cation potential.[38] In a more recent study[39] of seven alkali and alkaline earth silicate glass compositions using natural abundance ^{29}Si 2D MAF, we found that ^{29}Si shielding anisotropy of a Q^3 is linearly dependent on the Si–NBO bond length. The Si–NBO bond length, in turn, is linearly dependent on modifier cation potential. In the same study, we also found a systematic decrease in the Q^3 shielding anisotropy with increasing content of a given modifier, indicating a lengthening of the Si–NBO bond length which, in turn, was attributed to increasing NBO coordination by modifier cations, i.e., evidence for clustering at the short range.

While the Q^3 shielding anisotropy is primarily a probe of Si–NBO bond length, its correlation to the isotropic ^{29}Si chemical shift in a two-dimensional measurement dramatically enhances our ability to observe the distribution of Q^3 anisotropies present in a glass and, in principle, the distribution of Si–NBO bond lengths with changing composition. While this is not a direct probe of intermediate-range clustering, it can provide valuable structural constraints about the evolving random network with changing modifier content. Here we set out to investigate the dependence of the shielding anisotropy on changing mole fractions of network modifier cations in a binary alkali silicate glass. We chose cesium silicate compositions since cesium has a low cation potential leading to some of the largest ^{29}Si shielding anisotropies for Q^3 sites ($\zeta_\sigma \approx$ 70–90 ppm). Additionally, there is no evidence that Cs silicate glasses will undergo phase separation even at the highest silica contents examined here.

II. METHODS

A. Sample preparation

Ten samples were prepared from Cs_2CO_3 (Aldrich, 99+%) and SiO_2 (Aldrich, 99.995%) with the nominal composition $x\ Cs_2O{\cdot}(1-x)\ SiO_2$, where x were 0.14, 0.17, 0.18, 0.20, 0.22, 0.25, 0.29, 0.33, 0.36, and 0.40. Prior to synthesis the Cs_2CO_3 and SiO_2 were placed in a dehydrating oven at 150 °C overnight to remove any water from the materials. Approximately 0.5 wt. % CuO (Mallinckrodt) was added to each 2 g sample to enhance the longitudinal relaxation rate, $1/T_1$, of the nuclear magnetization. Copper(II) was chosen as it shortens the T_1 of the ^{29}Si nuclei without significantly shortening the ^{29}Si transverse relaxation time, T_2. This choice maintains our ability to enhance NMR sensitivity with echo train acquisition techniques such as Carr-Purcell-Meiboom-Gill (CPMG)[40–42] or Phase Incremented Echo Train Acquisition (PIETA).[43] The starting materials were ground about 10 min to obtain homogenous mixtures and placed in a furnace at 700 °C overnight to decarbonate followed by melting at the temperatures given in Table S1 of the supplementary material for 1–2 h. Each sample was quenched by placing the bottom of the platinum crucible in water. The resulted samples were fully transparent and possessed a uniform light blue color indicating that the copper is uniformly distributed.

Due to the low melting point (490 °C) and high volatility of Cs_2O the integrated areas of Q^n, resonances obtained from the ^{29}Si MAF spectrum (*vide infra*) were used to determine the final stoichiometric ratio of alkali metal oxide to silica in the final composition, $M_2O{\cdot}w\ SiO_2$. Combining the stoichiometric ratio

$$\frac{n_M}{n_{Si}} = \frac{2}{w} \tag{1}$$

with the charge balance equation

$$n_M = 4n_0 + 3n_1 + 2n_2 + n_3, \quad (2)$$

where n_M and n_n are the number of moles of metal oxide and Q^n species, respectively, one obtains the expression

$$w = \frac{2}{4y_0 + 3y_1 + 2y_2 + y_3}, \quad (3)$$

where y_n are the mole fractions taken as the integrated areas of the Q^n resonances given in Tables S4 and S5 of the supplementary material. This approach ignores the presence of free oxide (O^{2-}), which is not expected to be present in significant amounts in these silica-rich glass compositions.[44]

B. NMR measurements

NMR experiments were performed on a hybrid Tecmag Apollo-Chemagnetics CMX II 9.4 T (79.47 MHz for ^{29}Si) NMR spectrometer using 4 mm rotors in homebuilt dynamic-angle-spinning probes.[45] Rotor packing was performed in a nitrogen-filled glove bag. The sealed rotors were spun with compressed air dried to a dew point of −40 °C. Four dummy scans were performed before starting acquisition to establish a steady-state equilibrium and reduce differential relaxation. All experiments were performed at ambient temperature with spinning rates from 12 to 15 kHz.

The ^{29}Si relaxation time was measured for all glasses using the saturation recovery method[46] under magic-angle spinning (MAS). No evidence of differential relaxation among Q^n sites was observed in the saturation recovery measurements. The dominant nuclear spin relaxation mechanism for natural abundance ^{29}Si in bulk silicate glasses is expected to arise from through-space dipolar couplings to distant rapidly relaxing paramagnetic Cu(II) centers. In this mechanism, the ^{29}Si magnetization recovery is expected to follow a stretched exponential[47–50] and the magnetization recovery of the integrated spectrum (i.e., all Q^n sites) was fit to

$$S(t) = S_\infty \cdot \left[1 - \exp[-(t/T_1)^\beta]\right]. \quad (4)$$

The T_1 value, stretched exponent (β), and ^{29}Si longitudinal (75%) recovery times for each composition are given in Table S2 of the supplementary material. All relaxation data analyses give a β near 0.5 indicating that the paramagnetic relaxation agent was distributed uniformly through the glass.

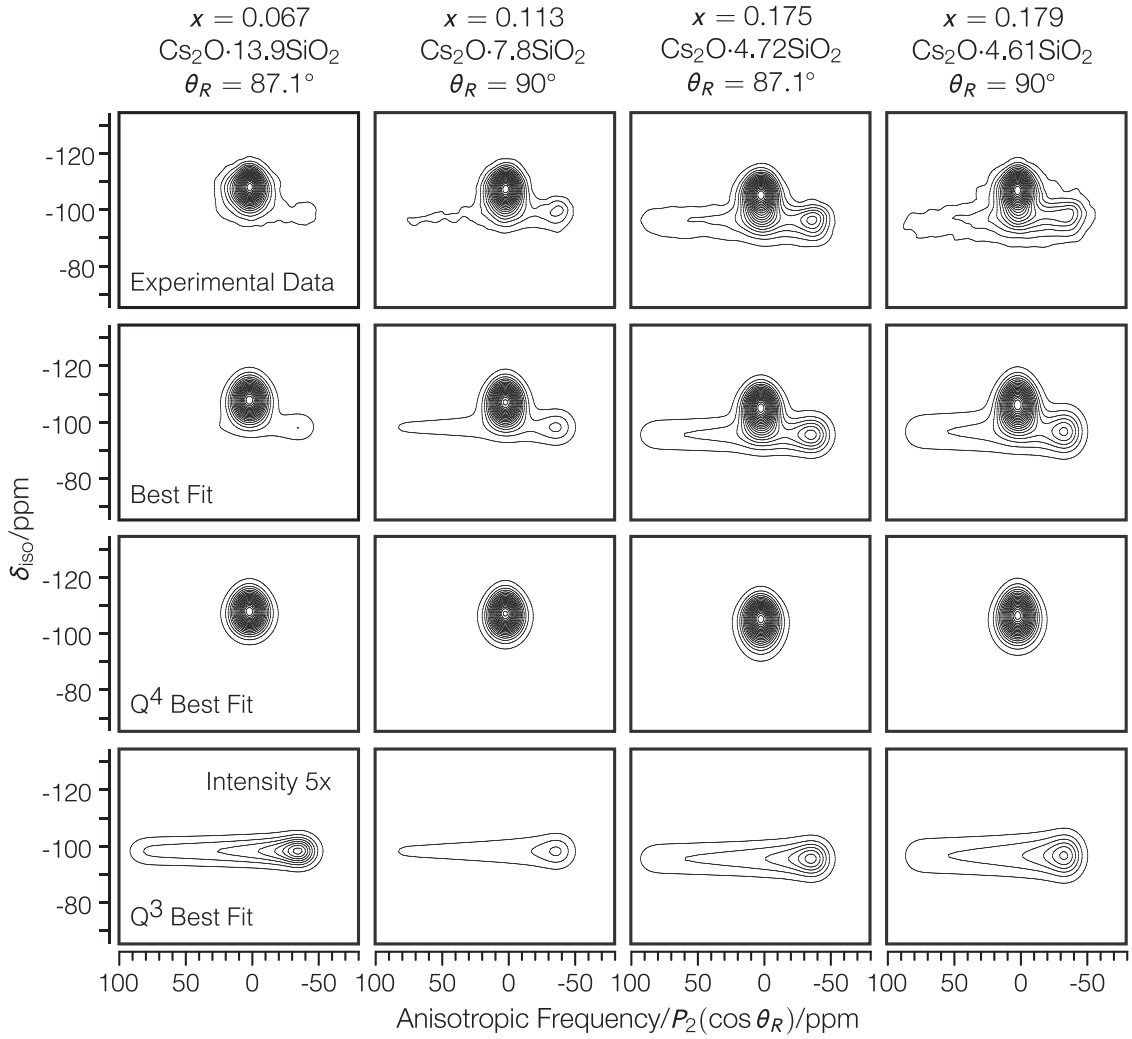

FIG. 1. Experimental 2D magic-angle flipping spectra (first row) for x = 0.067, x = 0.113, x = 0.175, and x = 0.179 with best fit spectra (second row), best fit Q^4 site (third row), and best fit Q^3 site (last row). The reduced χ^2 are 1.75, 1.39, 1.72, and 2.91, respectively. Twenty equally spaced contours are plotted from 3% to 96% of the maximum intensity. Isotropic frequencies in ppm are referenced to TMS. The anisotropic dimension is acquired at a rotor angle, θ_R.

A shifted-echo MAF pulse sequence with echo-train CPMG acquisition[40–42] was used and is described in a previous work.[39] This experiment correlates the MAS spectrum with an anisotropic off-magic-angle spectrum. The anisotropic dimension is acquired at a rotor angle, θ_R, nominally perpendicular to the applied field, where the anisotropic frequencies are scaled by a factor of $P_2(\cos\theta_R)$. Further experimental details are given in Table S3 of the supplementary material. The experimental 2D MAF spectra along with best-fit simulations are shown in Figs. 1–3.

All spectral processing, including affine transformations, were performed with *RMN*.[51] Following an approach outlined by Dey *et al.*,[42] the MAF signal with echo-train acquisition is converted into a three-dimensional signal with the echo train count, k, forming the third dimension. A matched stretched exponential filter is applied to the echo train dimension and the 3D signal is projected down to obtain the sensitivity enhanced 2D MAF signal. An active shear of the 2D time domain signal is applied parallel to the MAS dimension with a shear ratio of $\kappa = 1$. This leads to a signal correlating pure isotropic and anisotropic dimensions, leaving all anisotropic cross sections centered at 0 Hz.

C. 2D MAF line shape analysis

In this article, we employ the International Union of Pure and Applied Chemistry (IUPAC) definitions for the nuclear shielding and chemical shift interactions.[52] We use the notations $\zeta_\sigma^{(n)}$ and $\eta_\sigma^{(n)}$ to represent the nuclear shielding parameters for a Q^n site as described in our previous related studies.[38,39] The best-fit parameters from the least-squares analysis of each MAF spectrum are given in Tables S4–S6 of the supplementary material, for the isotropic chemical parameters of Q^4 sites, the isotropic chemical parameters of Q^3 and Q^2 sites, and the anisotropic chemical shift parameters of all Q^n sites, respectively. Details regarding the least-squares line shape analysis

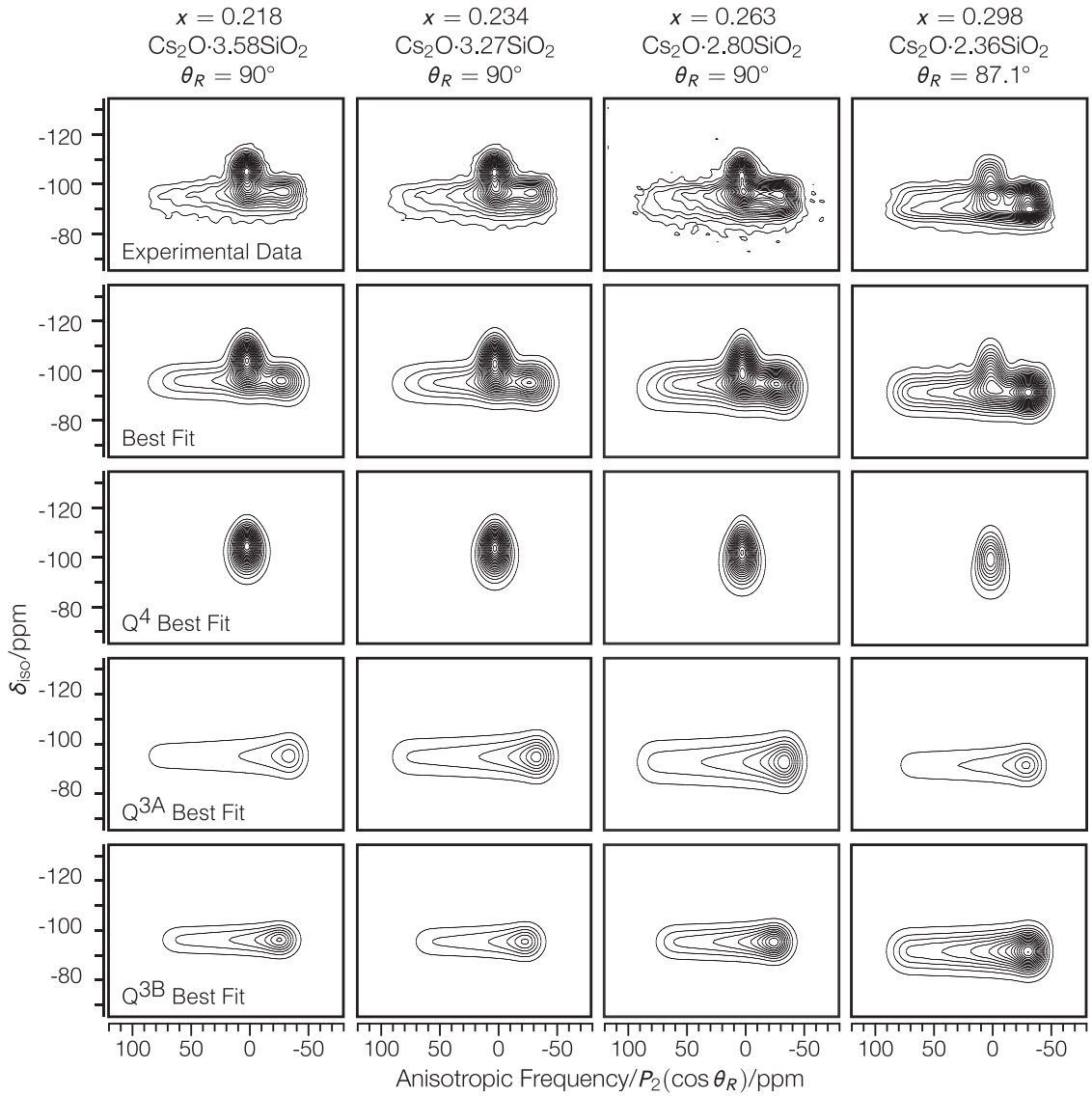

FIG. 2. Experimental 2D magic-angle flipping spectra (first row) for x = 0.218, x = 0.234, x = 0.263, and x = 0.298 with best fit spectra (second row), best fit Q^4 site (third row), and best fit Q^{3B} site (last row). The reduced χ^2 are 1.46, 1.61, 1.39, and 2.64, respectively. Twenty equally spaced contours are plotted from 3% to 96% of the maximum intensity. Isotropic frequencies in ppm are referenced to TMS. The anisotropic dimension is acquired at a rotor angle, θ_R.

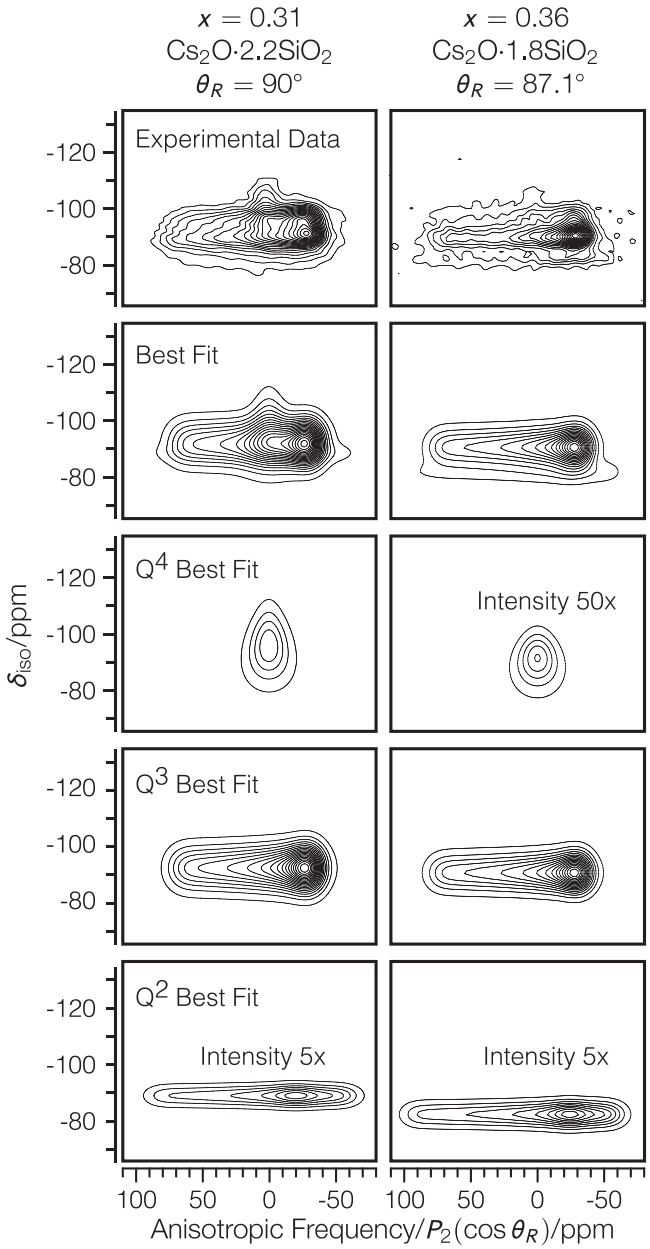

FIG. 3. Experimental 2D magic-angle flipping spectra (first row) for x = 0.31 and x = 0.36 with best fit spectra (second row), best fit Q^4 site (third row), best fit Q^3 site (fourth row), and best fit Q^2 site (last row). The averaged reduced χ^2 are 1.89, 3.66, and 1.23, respectively. Twenty equally spaced contours are plotted from 3% to 96% of the maximum intensity. Isotropic frequencies in ppm are referenced to TMS. The anisotropic dimension is acquired at a rotor angle, θ_R.

of the ^{29}Si MAF spectrum of silicate glasses are presented elsewhere.[39] Briefly, the 2D MAF line shape of the Q^4 resonances are modeled in the isotropic dimension as a skew-normal distribution,[53] defined as

$$S(\delta_{\mathrm{iso}}) = A \exp\left\{-\frac{1}{2}\left(\frac{\delta_{\mathrm{iso}} - \xi_{\mathrm{iso}}}{\Delta_{\mathrm{iso}}}\right)^2\right\} \times \left[1 + \mathrm{erf}\left(\frac{\alpha_{\mathrm{iso}}}{\sqrt{2}} \cdot \frac{\delta_{\mathrm{iso}} - \xi_{\mathrm{iso}}}{\Delta_{\mathrm{iso}}}\right)\right]. \quad (5)$$

The location ξ_{iso}, width Δ_{iso}, and shape α_{iso} of this distribution are later evaluated in terms of the more familiar parameters of the skew-normal distribution: the mean chemical shift, $\overline{\delta}_{\mathrm{iso}}$, the standard deviation, s_{iso}, the skewness, $\gamma_{1,\mathrm{iso}}$, and the excess kurtosis, $\gamma_{2,\mathrm{iso}}$. In the anisotropic dimension, the Q^4 resonances are modeled with a Gaussian distribution whose standard deviation, Δ_{aniso}, is made dependent on the correlated isotropic frequency, δ_{iso}, according to

$$\Delta_{\mathrm{aniso}}(\delta_{\mathrm{iso}}) = \Delta_0 + m_\Delta \cdot (\delta_{\mathrm{iso}} - \delta_{\mathrm{iso,\,mode}}), \quad (6)$$

where m_Δ is the linear slope for the variation of Δ_{aniso} and $\delta_{\mathrm{iso,mode}}$ is the mode of the Q^4 isotropic line shape. The value of m_Δ was found to increase from 0.03 ppm/ppm to 0.12 ppm/ppm with increasing Cs content. This serves to make each of the Q^4 peaks more triangular in shape in the 2D data with increasing Cs content as seen in Figs. 1–3. The anisotropic Gaussian broadening, Δ_0, was allowed to vary for the Q^4 sites. While it could vary, the fitting algorithm generally converged with an anisotropic width between 4.1 and 4.9 ppm at the peak with no real discernible trend.

For the Q^3 and Q^2 resonances, our model constrains the distribution of isotropic resonance frequencies to follow a normal distribution. Unlike Q^4, no improvements in the least-squares analysis were found on introducing a skew in their isotropic distributions. In the anisotropic dimension, the Q^3 and Q^2 resonances were modeled with an anisotropic chemical shift line shape broadened with a Gaussian convolution which was fixed at 7.80 ppm for Q^3 and Q^2 sites. Based on previous work,[35,37,54] the Q^3 anisotropic line shapes were further constrained to be axially symmetric (i.e., $\eta_\sigma = 0$).

A challenge in presenting uncertainties for the anisotropic shielding parameters arises from a strong covariance with the Gaussian line broadening that is also used in the least-squares analysis of anisotropic line shapes. The line broadening found during least-squares analysis of the anisotropic cross sections can be attributed to structural disorder, intrinsic excited state lifetime, and uncertainty in the tensor parameters. The uncertainties in the shielding tensor, therefore, can range from values as low as those reported in Table S6 of the supplementary material to as high as its corresponding Gaussian line broadening.

III. RESULTS AND DISCUSSION

Under static or off-magic angle spinning (MAS) conditions, each Q^n site exhibits an anisotropic ^{29}Si NMR line shape due to the anisotropy (CSA) of the chemical shift interaction.[35] This interaction arises from the magnetic shielding produced by the electron cloud surrounding the nucleus and reflects the nature and directionality of the bonding. It is characterized by three parameters: the isotropic chemical shift δ_{iso}, the nuclear shielding anisotropy ζ_σ, and the asymmetry parameter η_σ. The δ_{iso} parameter reflects the mean silicon environment, while ζ_σ measures the extent of the electron cloud distortion and η_σ expresses the departure from a cylindrically symmetric environment [$\eta_\sigma = 0$ (symmetric) → 1 (asymmetric)]. The Q^0 and Q^4 sites have the smallest anisotropy due to their highly symmetric environment. The remaining sites have relatively large anisotropies, with Q^3 and Q^1 sites having low asymmetry parameters which reflect the fact that their environment is close to axial symmetry. Under MAS conditions, where anisotropic broadening (i.e., information on ζ_σ and

η_σ) is removed, those five units are mainly identified only by their isotropic position, δ_{iso}, which approximately ranges from −70 ppm for Q^0 to −110 ppm for Q^4 with some considerable overlap.[55] Knowledge of all three tensor values, δ_{iso}, ζ_σ, and η_σ, as opposed to only δ_{iso} as measured under MAS conditions, provides a much more reliable method of separating overlapping isotropic (MAS) line shapes. There are numerous ways to obtain a two-dimensional (2D) isotropic/anisotropic correlation spectrum. We have adopted the magic-angle flipping method[35,56] where a MAS resonance is correlated to its static anisotropic line shape scaled by a factor of −0.5.

A. Overview of spectra

We begin by examining the overall changes in the 2D MAF spectra with changing cesium oxide content and then focus on the more subtle variations. In Fig. 1, we see that the 2D MAF spectrum of the glass composition with the lowest cesium oxide content, $x = 0.067$, is dominated by the Q^4 resonance centered on $\overline{\delta}_{iso} = -108.2$ ppm in the isotropic dimension with a weak Q^3 component appearing at $\overline{\delta}_{iso} = -98.8$ ppm which has a significantly broader resonance in the anisotropic dimension. As seen in Figs. 1–3, with increasing cesium oxide content, we observe the systematic decrease in the integrated area of Q^4 with a concomitant increase in the area of Q^3 resonances and the eventual appearance of Q^2 resonances. Most notable is the appearance of resonances with two distinctly different shielding anisotropies of approximately $\zeta_\sigma \approx 80$-90 ppm and $\zeta_\sigma \approx 65$-75 ppm—most prominent in the 2D MAF spectra of compositions $x = 0.263$ and $x = 0.298$ but also detected in the least-squares analyses of the compositions $x = 0.218$ and $x = 0.234$—as shown in Fig. 2. These two resonance types, both with $\eta_\sigma \approx 0$ are assigned to two distinctly different Q^3 environments (*vide infra*) and are labeled Q^{3A} and Q^{3B} for the larger and smaller anisotropic linewidths, respectively.

B. Q^3 disproportionation reaction

The integrated intensities of the Q^n species with changing cesium oxide content follow the expected behavior based on the model of Q^n disproportionation reactions[57,58] which take place in the melt,

$$2Q^3 \rightleftharpoons Q^2 + Q^4. \tag{7}$$

From the integrated areas of the Q^n signals, we can calculate the corresponding equilibrium constant,

$$k_3 = y_4\, y_2 / y_3^2, \tag{8}$$

where y_n is the mole fraction of the Q^n species. When k_3 is zero the population distribution of silicate tetrahedra within the glass is binary,[59–61] that is, the glass contains a maximum of two Q^n-species with the sequential appearance of other Q^n-species as the modifier cation content increases.[11] By contrast, calculated values of k_3, assuming a statistically random distribution[59–61] and neglecting the formation of free oxygen anion, would give $k_3 = 0.375$. Thus, one can view the equilibrium constants as a measure of frozen-in disorder or configurational entropy of the glass. In a glass with composition $x Cs_2O{\cdot}(1-x)SiO_2$, the mole fractions of all species in the equilibrium of Eq. (7) are given in Tables S4 and S5 of the supplementary material, the k_3 value was calculated to be $k_3 = 0.009 \pm 0.003$ for the $x = 0.31$ sample and $k_3 = 0.001 \pm 0.002$ for the $x = 0.36$ sample. Averaging these two measurements gives a $k_3 = 0.005 \pm 0.002$. A plot of the integrated areas of Q^n along with the trend predicted by $k_3 = 0.005$ is shown in Fig. 4. As would be expected for Cs^+, a cation with low field strength, the Q^n-species distribution is close to binary. This value of k_3 is in line with the trend (Fig. 7 in the work of Davis *et al.*[38]) with decreasing cation potential observed by Davis *et al.*[38] and in good agreement with the value obtained from Raman spectroscopy by Bykov *et al.*,[62] although slightly larger than the value reported by Malfait.[63]

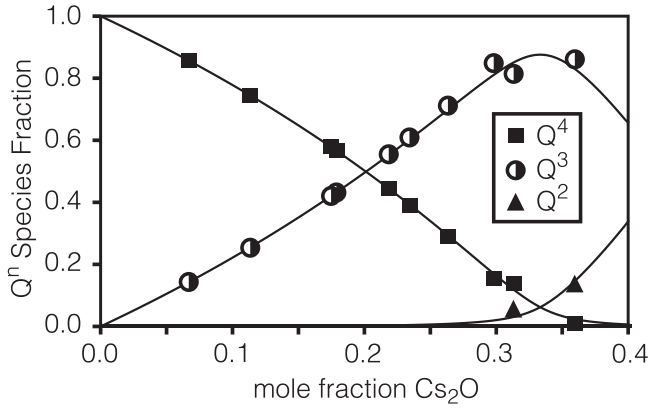

FIG. 4. Q^n species fraction as a function of Cs_2O mole fraction. The data were fitted to generate a disproportionation equilibrium constant, and the best agreement was obtained with $k_3 = 0.005$, drawn as solid black lines.

C. Isotropic shifts and widths

The isotropic projections of the best-fit simulated 2D spectra and the line shapes of the various Q^n species are shown together with the isotropic projection of the experimental 2D MAF spectra in Fig. 5. In Fig. 6, is a plot of the obtained mean chemical shift for each Q^n as a function of cesium oxide content. Here we observe a known trend[64] of Q^n isotropic chemical shift toward less negative (less shielded) values with increasing modifier content. For Q^4, the isotropic position is relatively constant near −108 ppm at high silica content and increases with increasing Cs content. Similar behavior is observed with the isotropic position of Q^3 initially remaining relatively constant near −99 ppm and again increasing at higher Cs mole fractions.

There are two established NMR parameter–structure relationships that give rise to this shift in isotropic position. First there is an approximately linear relationship between chemical shift on the mean Si–O–Si angle between Q^n sites causing the chemical shift to increase (less shielding) with decreasing mean Si–O–Si angle.[65,66] This effect explains, at best, a shift of no more than ∼6 ppm assuming the mean Si–O–Si angle varies between 150° and 140°. The second structural change causing the chemical shift to increase is changing the neighboring tetrahedra[28,67] from Q^4 to Q^3, that is, starting from silica rich compositions and increasing the Cs content the predominant Q^4 sites change from $Q^{4,4444}$ to $Q^{4,4443}$ to $Q^{4,4433}$ to $Q^{4,4333}$ to $Q^{4,3333}$. Here the notation $Q^{4,4444}$

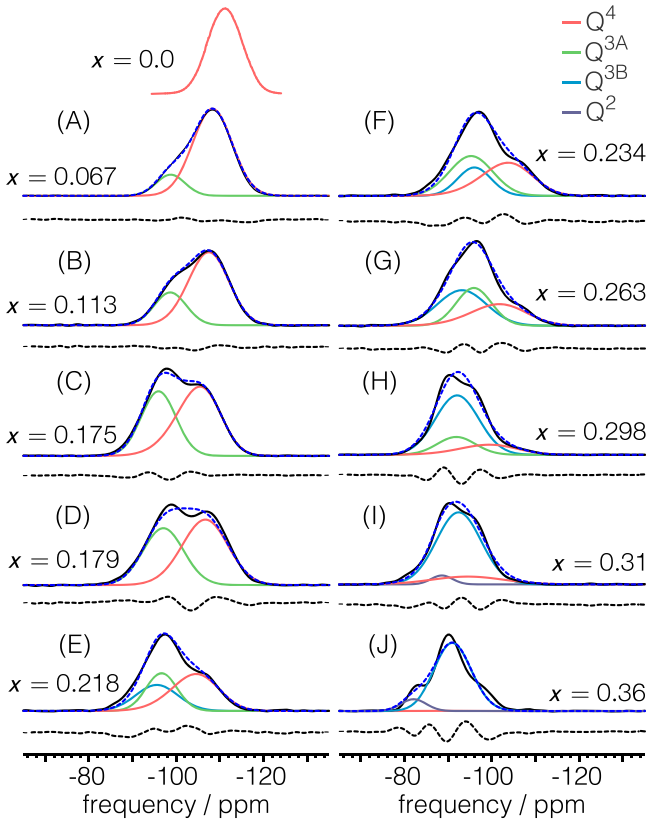

FIG. 5. Isotropic projections of the experimental 2D spectra, shown as black line, and isotropic projections of the best-fit simulated 2D spectra, shown as dashed blue line (a) $Cs_2O{\cdot}13.9\ SiO_2$, (b) $Cs_2O{\cdot}7.8\ SiO_2$, (c) $Cs_2O{\cdot}4.72\ SiO_2$, (d) $Cs_2O{\cdot}4.61\ SiO_2$, (e) $Cs_2O{\cdot}3.58\ SiO_2$, (f) $Cs_2O{\cdot}3.27\ SiO_2$, (g) $Cs_2O{\cdot}2.80\ SiO_2$, (h) $Cs_2O{\cdot}2.36\ SiO_2$, (i) $Cs_2O{\cdot}2.2\ SiO_2$, (j) $Cs_2O{\cdot}1.8\ SiO_2$. The individual Q^n components' isotropic line shapes obtained from the analysis of the corresponding 2D MAF spectra are shown as colored lines. Also shown in each plot is the difference between experimental and best-fit projections.

represents a Q^4 unit connected to four other Q^4 units, as in silica glass SiO_2, while $Q^{4,4333}$ represents a Q^4 unit connected to one Q^4 unit and three Q^3 units. Similarly, the increase in Q^3 chemical shift with increasing Cs content arises due to the shifting predominance of anionic clusters from $Q^{3,444}$ to $Q^{3,443}$ to $Q^{3,433}$ to $Q^{3,333}$. In previous NMR studies of binary sodium silicate glasses, ranging in sodium oxide mole fractions from $x = 0.15$ to $x = 0.25$, Olivier *et al.*[28] observed a shift of −112 ppm to −101.5 ppm from $Q^{4,4444}$ to $Q^{4,3333}$, respectively, and a shift of −97 ppm to −89 ppm from $Q^{3,444}$ to $Q^{3,333}$, respectively. This is similar to the range of shifts observed in Fig. 6 over the same range of cesium oxide mole fractions. This behavior is also consistent with that observed by Malfait *et al.*[68] in ^{29}Si NMR measurements of potassium silicate glasses.

In Fig. 7, we see a less established trend toward increased Q^n isotropic line width with increasing cesium oxide content. In the case of Q^4, the standard deviation of the isotropic line shape increases with increasing Cs content from approximately 4.5–6.6 ppm, and, in the case of Q^3, from approximately 3–5 ppm. In the case of Q^4, it is interesting to note that the line width is the widest at the highest Cs content where Q^4 concentrations are the lowest but still detectable. In a structural model where the next nearest neighbors of each Q^4 are a random mix of the available Q^n species, one would expect the

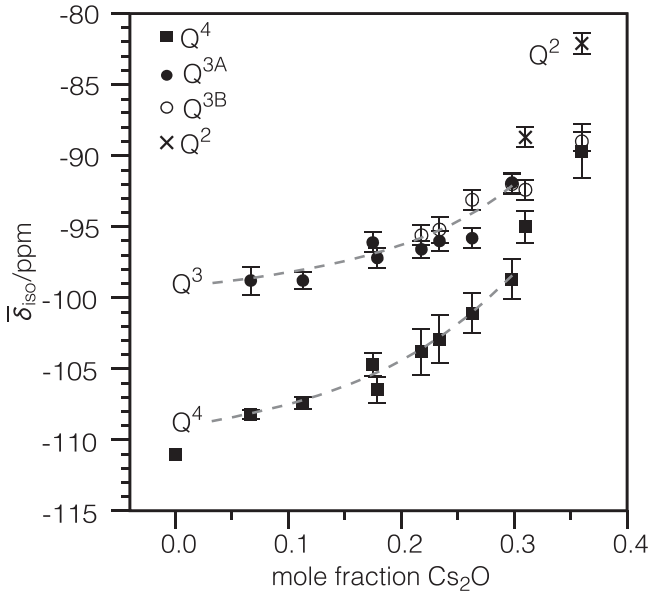

FIG. 6. Mean isotropic chemical shift of the isotropic line shape for Q^4 and Q^3 as a function of mole fraction. The dashed lines are the mean isotropic chemical shifts obtained from the simulations assuming the random connectivity model.

resonance to be dominated by $Q^{4,3333}$ at such high Cs concentrations. Furthermore, one might presume that such a uniform coordination environment would lead to a narrower Q^4 line width than what is experimentally observed.

To explore a possible explanation for the behavior of the Q^4 isotropic shape extracted from each MAF spectrum, we model the Q^4 isotropic line shape as consisting of 5 strongly overlapping Gaussian resonances associated with $Q^{4,4444}$, $Q^{4,4443}$, $Q^{4,4433}$, $Q^{4,4333}$, and $Q^{4,3333}$, each having isotropic positions and line widths independent of the Cs content and relative amplitudes, $A_4(r)$, fixed according to a random connectivity model[69,70] (RCM). Following the treatment by Machacek *et al.*[70] in the simple case where only Q^4 and Q^3 species are present in the glass, we first define the probabilities that a randomly chosen connection between adjacent Q^n includes a Q^3 or Q^4 as

$$\pi_3 = \frac{3y_3}{3y_3 + 4y_4}, \quad \pi_4 = \frac{4y_4}{3y_3 + 4y_4}, \tag{9}$$

respectively. Here y_3 and y_4 are the Q^3 and Q^4 probabilities experimentally determined as a function of Cs content and also given in Table S4 of the supplementary material. The probability for a given $Q^{4,ijkl}$ site is then calculated from the binomial distribution according to[70]

$$A_4(r) = y_4 \frac{4!}{r!(4-r)!} \pi_4^r \pi_3^{4-r}, \tag{10}$$

where r is the number of neighboring Q^4 tetrahedra. The corresponding model for the $x = 0.31$ and $x = 0.36$ compositions, where Q^2 sites present, requires a trinomial distribution, leading to a total of 15, 10, and 6 different possibilities for Q^4, Q^3, and Q^2 sites, respectively. This leads to a larger and unreliable number of fit parameters; thus this analysis was not considered further.

The extracted Q^4 isotropic line shapes from glass compositions where Q^4 and Q^3 are the only anionic species present

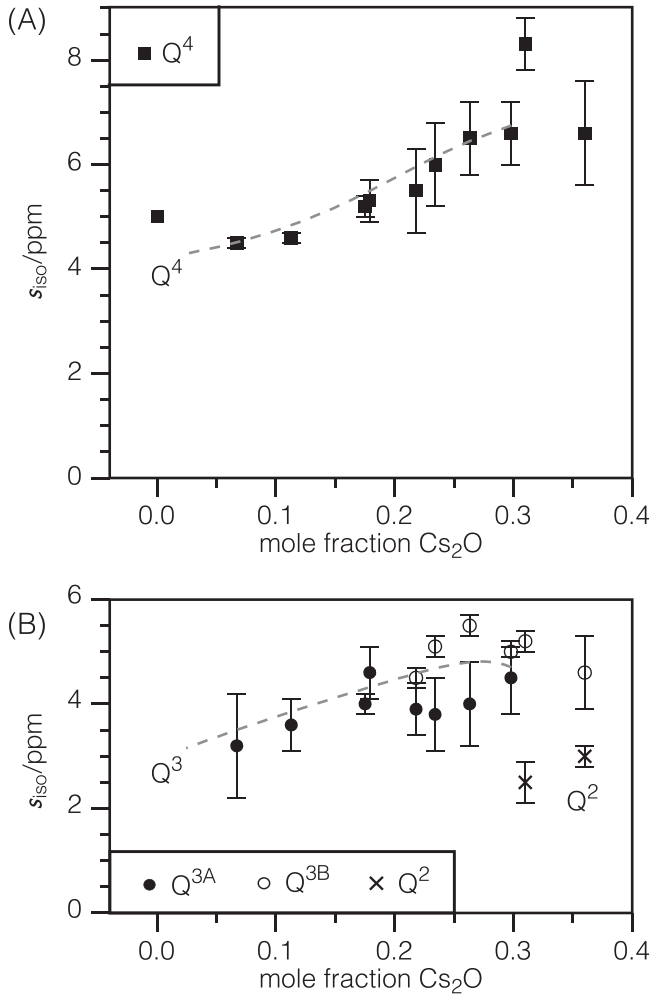

FIG. 7. Standard deviation of the isotropic line shape for (a) Q^4 and (b) Q^3 and Q^2, as a function of mole fraction. The dashed gray lines are the standard deviations obtained from the simulations assuming the random connectivity model.

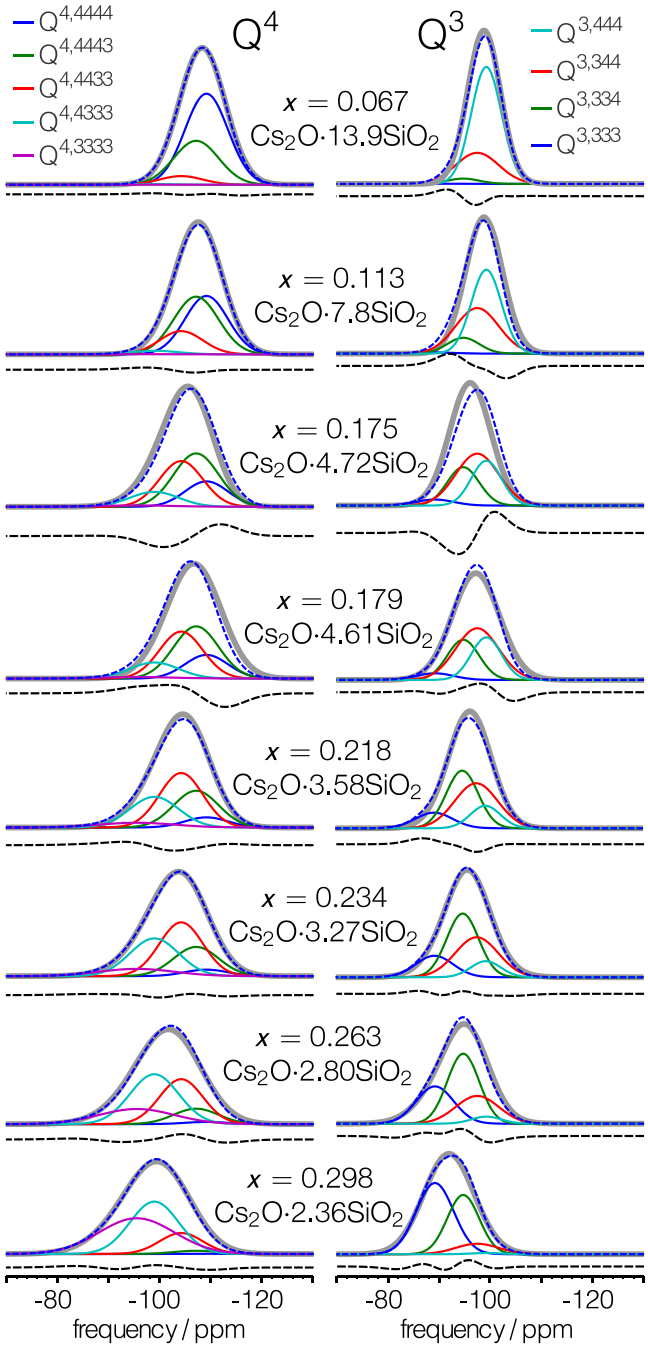

FIG. 8. The thick gray line is the isotropic 1D projections of the best-fit simulated 2D spectra of the Q^4 (left) and Q^3 (right) species. The dashed blue line is the predicted overall line shape composed of five and four distinct Gaussian resonances ($Q^{n,ijk(l)}$, shown as colored lines), respectively, for Q^4 (left) and Q^3 (right), whose integrated intensities are fixed by the predictions of RCM as given in Table S7 of the supplementary material. Also shown below each as a black dashed line are the residuals between the isotropic line shape and RCM predicted model.

($x \leq 0.298$) are shown as the thick solid gray line in the spectra of the left column of Fig. 8. The best-fit model overall line shape is shown as the dashed blue line in the Q^4 isotropic spectra of the left column of Fig. 8 along with the five component, $Q^{4,ijkl}$, line shapes as solid color lines. Below each composition model line shapes are the residuals between the overall line shape and model as a black dashed line. The 10 best-fit model parameters: the 5 isotropic positions and 5 standard deviations of the $Q^{4,ijkl}$ are given in Table S7 of the supplementary material. The individual $Q^{4,ijkl}$ positions in Table S7 of the supplementary material are consistent with previous explanations and observations of less negative chemical shifts with increasing number of Q^3 neighbors.[28]

The predicted trend in mean isotropic chemical shift of Q^4 using RCM, shown as the dashed line in Fig. 6, gives good agreement with the experimental trend. Additionally, good agreement with experiment is obtained with the predicted increase in the standard deviation of the Q^4 line shape with increasing Cs content using RCM, shown as the dashed line in Fig. 7(a). It is difficult to assess the structural origin of the increased $Q^{4,ijkl}$ line width with increasing number of Q^3 neighbors. One possibility is that there is an increase in the degree of random distortions away from tetrahedral symmetry around the Q^4 sites as the network becomes depolymerized.

The random RCM distribution of Q^3 and Q^4 in the second-coordination of a Q^4 implies not only the absence of phase separation but also the absence of any degree of preferential assembly of the cesium cations. While the first implication is reasonable, as no phase separation is expected in a cesium

silicate glass, the second might raise some eyebrows, as experimental observations tend to indicate some degree of modifier cation clustering in silicate glasses.[15] Our assumptions, however, are consistent with the experimental findings of Sen and Youngman,[71] who reported random distribution of Q^n species in potassium silicate glasses. Furthermore, Machacek *et al.*[70] re-analyzed the 2D NMR correlation experiments on ^{29}Si-enriched sodium silicate glasses by Olivier *et al.*[28] using the RCM model and also obtained reasonable agreement with experimental results.

In the right column of Fig. 8, we show the results of a similar analysis of the extracted Q^3 isotropic line shapes from glass compositions where Q^4 and Q^3 are the only anionic species present. Here we model the evolution of the Q^3 isotropic line shapes as consisting of 4 strongly overlapping Gaussian resonances associated with $Q^{3,444}$, $Q^{3,443}$, $Q^{3,433}$, and $Q^{3,333}$, each having isotropic positions and line widths independent of the Cs content and relative amplitudes, $A_3(r)$, fixed according to the RCM distribution

$$A_3(r) = y_3 \frac{3!}{r!(3-r)!} \pi_3^r \pi_4^{3-r}, \tag{11}$$

where r is the number of neighboring Q^4 tetrahedra. In this analysis, the peaks for Q^{3A} and Q^{3B} were added together to one entity. This is reasonable as there are no large differences in the extracted Q^3 isotropic line shapes after the appearance of the second species. Furthermore, the co-existence of Q^{3A} or Q^{3B} anisotropic line shapes with identical isotropic shifts suggests that there is no correlation between the identity of neighboring Q^n sites and whether a Q^3 unit is Q^{3A} or Q^{3B}.

The RCM predicted mean Q^3 chemical shift with increasing Cs content gives good agreement with the experimental trend and is shown as the dashed line for Q^3 in Fig. 6. The individual $Q^{3,ijk}$ line widths (standard deviations) given in Table S7 of the supplementary material also increase with increasing Cs content. The predicted standard deviation of the line shapes with increasing Cs content also gives good agreement with the experimental trend and is shown as the dashed line in Fig. 7(b). The range of $Q^{3,ijk}$ line widths is smaller than those of the $Q^{4,ijkl}$ sites. This smaller range could be attributed to either the Q^3 experiencing a lesser degree of random distortions away from the local C_{3v} symmetry of Q^3 sites as the network becomes depolymerized or could simply be that the ^{29}Si isotropic chemical shift of Q^3 is less sensitive to random distortions than that of Q^4.

D. Two distinct Q^3 sites

In the four MAF spectra in Fig. 2, we observe evidence for two distinctly different shielding anisotropies of approximately $\zeta_\sigma \approx$ 80-90 ppm and $\zeta_\sigma \approx$ 65-75 ppm, both with $\eta_\sigma \approx 0$. Note that fits on the x = 0.218, 0.234, 0.263, and 0.298 spectra assuming a single site resulted in increased values of χ^2_ν by factors of 2–3. Additional evidence for two Q^3 sites is seen in partial projections onto the isotropic dimension that exclude the Q^4 resonance. Such partial projections over a range of −50 ppm to −20 ppm in the anisotropic dimension of Fig. 2 are shown in Fig. 9. Clearly, neither isotropic projection is the result of a single Gaussian peak.

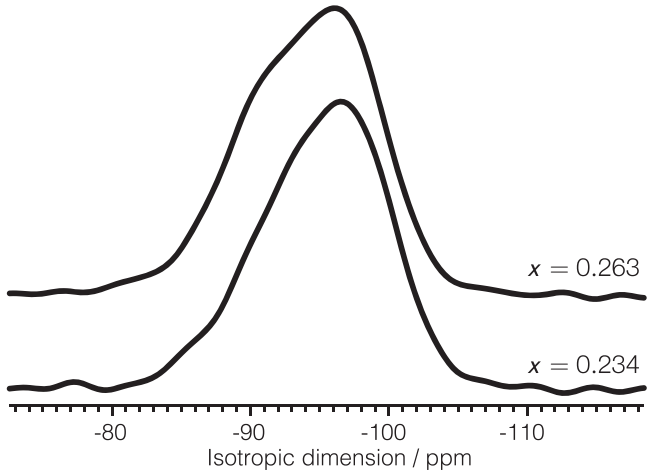

FIG. 9. Partial projection of Q^3 region onto the isotropic dimension (−50 ppm to −20 ppm in the anisotropic dimension) for the x = 0.26 and x = 0.23 datasets.

In Fig. 10 is a plot of the shielding anisotropy of the Q^3 sites as a function of Cs content. As noted earlier, we set out to investigate the dependence on shielding anisotropy on changing mole fraction of network modifier cation—choosing cesium silicate compositions since they have one of the largest ^{29}Si shielding anisotropy for Q^3 sites ($\zeta_\sigma \approx$ 70–90 ppm). By increasing Cs content, we expect that increased modifier clustering around the NBO would lead to a decrease in the Q^3 shielding anisotropy. This is indeed the approximate trend that we observe in the anisotropies in Fig. 10. At the highest silica content, where only 14% of Q^n in the glass are Q^3, we observe a shielding anisotropy of ~90 ppm. With increasing Cs content the shielding anisotropies steadily decrease, reaching a value of 73 ppm at x = 0.36. Unexpected was the appearance of a second Q^3 site at x = 0.218 with markedly smaller shielding anisotropy (labeled Q^{3B}) coexisting with the Q^3 site having a larger anisotropy (Q^{3A}). The two different Q^3 environments, the open and closed circles, at lower Cs content, gradually become a single environment (Q^{3B}) at higher Cs content.

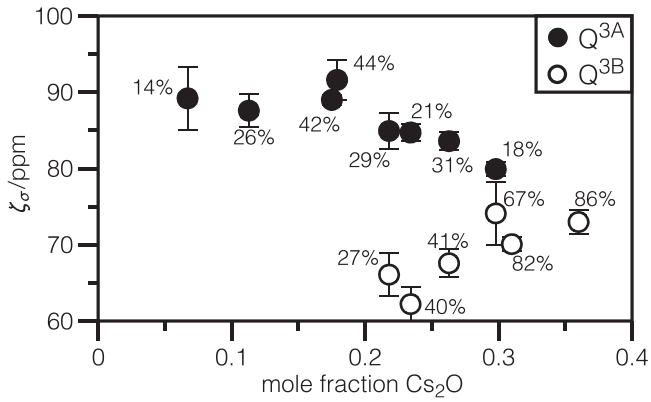

FIG. 10. Chemical shift anisotropy, ζ_σ, as a function of Cs_2O mole fraction plot with Q^3 site compositions in percentage. The Q^3 site compositions were calculated from the single Q^n site best fits shown in third, fourth, and fifth rows of Figs. 1–3. At x = 0.218 a second, structurally distinct, Q^3 site appears. At higher concentratons Q^{3B} gradually replaces Q^{3A} until no Q^{3A} sites are detected.

In our previous work,[39] we found that the Q^3 shielding anisotropy was linearly dependent on the length of the Si–NBO bond with decreasing anisotropy as the Si–NBO bond lengthened. Furthermore, we found that the Si–NBO bond length, in turn, is linearly dependent on cation potential (Z/r) and the number of coordinating modifier cations. The linear dependence of the shielding anisotropy on Si–NBO length is well known and dates back to the work by Grimmer and coworkers[54,72] in the early 1980s and similarly confirmed by Kirkpatrick and others[73,74] in phosphate glasses. The explanation for dependence on the Si–NBO length on the nature and number of modifier cations dates back to Pauling's *Nature of the Chemical Bond*.[75] There is a linear relationship between the Si–NBO length and the electronegativity of the NBO, which, in turn, is linearly dependent on the electronegativity of the modifier cation. The larger the electronegativity of the modifier cation, the longer the Si–NBO bond (Si has larger electronegativity than any alkali or alkaline earth; therefore, Si–BO are longer than Si–NBO). This explanation holds for both the varying cation potential and varying coordination number of the modifier cations. On this basis and the value of $\eta_\sigma \approx 0$ for Q^{3A} and Q^{3B} sites we assign these two resonances to sites with distinctly different Si–NBO lengths—the larger ζ_σ is assigned to the Q^{3A} with the shorter Si–NBO length and the smaller ζ_σ is assigned to the Q^{3B} with the longer Si–NBO length. This structural assignment is not without precedent. Both Osipov *et al.*[76] and O'Shaughnessy *et al.*[77] studied cesium silicates with Raman spectroscopy and, while their peak assignment has strong discrepancies, both postulate the existence of a second site (at completely different frequencies). Osipov *et al.*[76] attributed both sites to different Si–NBO bond lengths and explained this difference by the number of Q^4 neighbors ($Q^{3,444}$ and $Q^{3,443}$ vs. $Q^{3,433}$ and $Q^{3,333}$). O'Shaughnessy *et al.*[77] also attributed the differences between both Q^3 sites to the number of cations in close proximity.

We can take our analysis of the Q^{3A} and Q^{3B} sites further by proposing an approximate quantitative relationship between Q^3 anisotropy and Si–NBO length,

$$\zeta_\sigma = m(d_{\mathrm{Si-BO}} - d_{\mathrm{Si-NBO}}),$$

where $d_{\mathrm{Si-BO}}$ and $d_{\mathrm{Si-NBO}}$ are the Si–O lengths involving the bridging and non-bridging oxygen on a Q^3, respectively. A Si–O length typically varies from ~1.55 Å to ~1.60 Å in going from Si–NBO to Si–BO. A simple approximation is to assume the ζ_σ value of ~75 ppm measured in the disilicate composition correlates to an Si–NBO length of 1.55 Å. Further assuming $d_{\mathrm{Si-BO}}$ to be 1.60 Å yields a slope of m = 1500 ppm/Å. With this slope we can assign the shielding anisotropies of 85 ppm and 62 ppm at $x = 0.234$ for Q^{3A} and Q^{3B}, respectively, to Si–NBO lengths of 1.54 Å and 1.59 Å. The ~22 ppm difference between Q^{3A} and Q^{3B} anisotropies corresponds to 0.015 Å, that is, Q^{3B} has a Si–NBO that is 0.015 Å longer than Q^{3A}. From this we would also deduce that the highest shielding anisotropy of ~90 ppm at the highest silica content corresponds to a Si–NBO length of 1.54 Å.

The appearance of the coexisting sites at a mole fraction of $x = 0.218$ strongly suggests a connection to a percolation threshold. It has been argued in silicate glasses that the fraction of non-bridging oxygens to the total number of oxygens can be used to explain observed responses in terms of critical percolation thresholds[19] (see discussion in the Introduction). For simplification, we treat the glass as a network of random closed packed BO and NBO, both having equal volumes. In that case, the critical concentration for percolation is reached when 27% of all oxygens are NBO, which is equivalent to a Q^3 fraction of $y_3 = 62\%$ or a Cs_2O mole fraction of $x = 0.24$. Based on the closeness of this critical mole fraction to the mole fraction at which the second Q^{3B} site appears, we hypothesize that the appearance of the Q^{3B} site is associated with the formation of the infinitely extended (spanning) percolation cluster of NBO. This infinitely extended cluster contains the channels responsible for ionic diffusion. The high density of Cs^+ in the percolation channels lead to higher Cs^+ coordination around the NBO of the Q^{3B} site with its correlated longer Si–NBO bond length. The Q^{3A} site would then be associated with the finite size modifier clusters. The finite size clusters are associated with regions of a lower density of Cs^+ and lower coordination around the NBO of the Q^{3A} site with its correlated shorter Si–NBO bond length. Only finite size clusters exist in the glass before the percolation threshold is reached. At the lowest Cs contents, we expect the cluster size distribution to be dominated by isolated NBO coordinated by a single Cs^+.

Finally, we note that the Q^{3B} shielding anisotropy, shown as open circles in Fig. 10, first appears with a value of 66.1 ppm at $x = 0.218$ and gradually increases with increasing Cs content to 73 ppm at $x = 0.36$. This implies that the Q^{3B} Si–NBO lengths in the infinitely extended cluster decrease with increasing Cs content. The simple percolation argument put forth so far assumes an unchanging random close packed geometry. With increasing Cs content, however, we expect the random silicate network to become further depolymerized. Thus, we believe that the increasing Q^{3B} shielding anisotropy (and decreasing Si–NBO bond length) arises from a corresponding decrease in the smaller ring sizes and a less tight packing of Cs cations around NBO. O'Shaughnessy *et al.*[77] also noted important changes in binary cesium silicates at Cs_2O mole fractions of approximately 20%, including a sharp decrease in the number of three-membered rings and of Q^n species in proximity of multiple cations with increasing Cs content.

IV. SUMMARY

In this paper, we present and analyze the natural abundance ^{29}Si 2D magic-angle flipping NMR spectra of ten $xCs_2O{\cdot}(1-x)SiO_2$ glasses where x was varied from 0.067 to 0.36. Through detailed analyses of the two-dimensional line shapes we can draw a number of conclusions about the evolution of the atomic-level structure with increasing modifier content.

The most surprising result is the observation of two coexisting Q^3 sites in a Cs_2O mole fraction interval between $x = 0.218$ and $x = 0.298$. Based on our previous work,[39] we can distinguish these two sites as having longer and shorter Si–NBO bond lengths. By most accounts one would interpret such an observation as evidence of some form of phase separation, except in this case the glass sample composition is a

cesium silicate—in which one hardly expects to see any signs of phase separation. An important clue in devising an explanation of this result is that the coexisting sites first appear at a Cs_2O mole fraction suspiciously close to the critical percolation threshold predicted by the critical occupied volume fraction of Scher and Zallen,[14,16,17] $\phi_c = 0.16$, for a random close packing of oxygen. In this case, the critical concentration for percolation is reached when 27% of all oxygens are NBO, which is equivalent to a Cs_2O mole fraction of $x = 0.24$—a value surprisingly close to the mole fraction at which the second Q^3 site appears ($x = 0.218$). Thus, the shorter Si–NBO bond length site, labeled Q^{3A}, is associated with the finite size modifier clusters in regions of a lower Cs^+ density, and thus has a lower Cs^+ coordination around the NBO and a corresponding shorter Si–NBO bond length. The longer Si–NBO bond length, labeled Q^{3B}, is associated with the formation of the infinitely extended (spanning) percolation cluster of modifiers. It is the higher Cs^+ coordination around the NBO of the Q^{3B} sites in the percolation channels of the infinite cluster that results in a longer Si–NBO bond length. Moreover, we find that further depolymerization of the random silicate network with increasing Cs content beyond the percolation threshold leads to a shortening of the Si–NBO bond length of the Q^{3B} site, making it less distinguishable from the Q^{3A} associated with the finite modifier cluster sizes.

The 2D ^{29}Si MAF also allows the MAS line shapes to be decomposed with significantly greater accuracy than can be obtained with 1D MAS spectrum alone. From our analysis of the evolution of isotropic ^{29}Si MAS line shapes with increasing Cs content, we conclude that the next nearest neighbors of Q^4 and Q^3 are drawn randomly from the Q^n tetrahedra present in the glass. The isotropic ^{29}Si MAS line shape analysis also suggests an increase in the degree of random distortions away from tetrahedral symmetry around the Q^4 sites as the network becomes depolymerized.

Although the results are evidence for different degrees of modifier cation clustering, the evolution of the modifier cation distribution in cesium silicate glass with increasing Cs content appears entirely consistent with the continuous random network (CRN) structural model,[11,12] where "random" is interpreted in the context of percolation theory.[14] At the same time, these results indicate significant deviation from "random" in that there is considerable order in the distribution of anionic species, Q^n, which is shown to follow the binary distribution model.[59,60] Despite the strong order in the Q^n-species distribution, the connectivities between Q^n follow the random connectivity model[69,70]—a result that is entirely consistent with the random evolution of the modifier cation distribution.

SUPPLEMENTARY MATERIAL

See supplementary material for additional tables and details on the sample preparation, sample characterization, and spectral analysis.

ACKNOWLEDGMENTS

This material is based upon work supported in part by the National Science Foundation under Grant No. CHE-1506870. The authors would like to thank Dr. Pierre Florian for helpful discussions during the early stages of this work and Professor Sabyasachi Sen for helpful discussions on percolation theory.

[1] J. Shelby, *Introduction to Glass Science and Technology*, RSC Paperbacks Series (Royal Society of Chemistry, 2005).
[2] A. K. Varshneya, *Fundamentals of Inorganic Glasses* (Academic Press, Inc., San Diego, CA, 1994).
[3] G. N. Greaves, S. J. Gurman, C. R. A. Catlow, A. V. Chadwick, S. Houde-Walter, C. M. B. Henderson, and B. R. Dobson, Philos. Mag. A **64**, 1059 (1991).
[4] M. D. Ingram, Philos. Mag. B **60**, 729 (1989).
[5] P. Maass, A. Bunde, and M. D. Ingram, Phys. Rev. Lett. **68**, 3064 (1992).
[6] J. O. Isard, J. Non-Cryst. Solids **1**, 235 (1969).
[7] D. E. Day, J. Non-Cryst. Solids **21**, 343 (1976).
[8] P. Maass, J. Non-Cryst. Solids **255**, 35 (1999).
[9] G. N. Greaves and S. Sen, Adv. Phys. **56**, 1 (2007).
[10] J. C. Dyre, P. Maass, B. Roling, and D. L. Sidebottom, Rep. Prog. Phys. **72**, 046501 (2009).
[11] W. H. Zachariasen, J. Am. Chem. Soc. **54**, 3841 (1932).
[12] B. E. Warren and J. Biscoe, J. Am. Ceram. Soc. **21**, 259 (1938).
[13] S. R. Broadbent and J. M. Hammersley, Math. Proc. Cambridge Philos. Soc. **53**, 629 (1957).
[14] R. Zallen, *The Physics of Amorphous Solids* (Wiley, New York, 1983).
[15] G. N. Greaves, J. Non-Cryst. Solids **71**, 203 (1985).
[16] H. Scher and R. Zallen, J. Chem. Phys. **53**, 3759 (1970).
[17] R. Zallen, "The sixteen-percent solution: Critical volume fraction for percolation," in *Phase Transitions and Self-Organization in Electronic and Molecular Networks* (Springer US, Boston, MA, 2001), pp. 37–41.
[18] Y. Liang, F. M. Richter, A. M. Davis, and E. Bruce Watson, Geochim. Cosmochim. Acta **60**, 4353 (1996).
[19] S. Sen and T. Mukerji, Geophys. Res. Lett. **24**, 1015, https://doi.org/10.1029/97gl00924 (1997).
[20] K. Otto and M. Milberg, J. Am. Ceram. Soc. **50**, 513 (1967).
[21] K. Otto and M. Milberg, J. Am. Ceram. Soc. **51**, 326 (1968).
[22] P. H. Gaskell, M. C. Eckersley, A. C. Barnes, and P. Chieux, Nature **350**, 675 (1991).
[23] I. Farnan, P. J. Grandinetti, J. H. Baltisberger, J. F. Stebbins, U. Werner, M. A. Eastman, and A. Pines, Nature **358**, 31 (1992).
[24] P. Florian, K. E. Vermillion, P. J. Grandinetti, I. Farnan, and J. F. Stebbins, J. Am. Chem. Soc. **118**, 3493 (1996).
[25] J. F. Stebbins, J. V. Oglesby, and Z. Xu, Am. Mineral. **82**, 1116 (1997).
[26] S. K. Lee and J. F. Stebbins, J. Phys. Chem. B **107**, 3141 (2003).
[27] J. R. Allwardt and J. F. Stebbins, Am. Mineral. **89**, 777 (2004).
[28] L. Olivier, X. Yuan, A. N. Cormack, and C. Jäger, J. Non-Cryst. Solids **293-295**, 53 (2001).
[29] B. Gee, M. Janssen, and H. Eckert, J. Non-Cryst. Solids **215**, 41 (1997).
[30] B. Gee and H. Eckert, J. Phys. Chem. **100**, 3705 (1996).
[31] L. Wüllen, B. Gee, L. Züchner, M. Bertmer, and H. Eckert, Ber. Bunsengesellschaft Phys. Chem. **100**, 1539 (1996).
[32] U. Voigt, H. Lammert, H. Eckert, and A. Heuer, Phys. Rev. B **72**, 064207 (2005).
[33] S. Peter Puls and H. Eckert, Phys. Chem. Chem. Phys. **9**, 3992 (2007).
[34] H. Eckert, Z. Phys. Chem. **224**, 1591 (2010).
[35] P. Zhang, C. Dunlap, P. Florian, P. J. Grandinetti, I. Farnan, and J. F. Stebbins, J. Non-Cryst. Solids **204**, 294 (1996).
[36] P. Zhang, P. J. Grandinetti, and J. F. Stebbins, J. Phys. Chem. B **101**, 4004 (1997).
[37] M. Davis, D. C. Kaseman, S. M. Parvani, K. J. Sanders, P. J. Grandinetti, P. Florian, and D. Massiot, J. Phys. Chem. A **114**, 5503 (2010).
[38] M. Davis, K. J. Sanders, P. J. Grandinetti, S. J. Gaudio, and S. Sen, J. Non-Cryst. Solids **357**, 2787 (2011).
[39] J. H. Baltisberger, P. Florian, E. G. Keeler, P. A. Phyo, K. J. Sanders, and P. J. Grandinetti, J. Magn. Reson. **268**, 95 (2016).
[40] H. Y. Carr and E. M. Purcell, Phys. Rev. **94**, 630 (1954).
[41] S. Meiboom and D. Gill, Rev. Sci. Instrum. **29**, 688 (1958).
[42] K. Dey, J. T. Ash, N. M. Trease, and P. J. Grandinetti, J. Chem. Phys. **133**, 054501 (2010).
[43] J. H. Baltisberger, B. J. Walder, E. G. Keeler, D. C. Kaseman, K. J. Sanders, and P. J. Grandinetti, J. Chem. Phys. **136**, 211104 (2012).
[44] J. F. Stebbins and S. Sen, J. Non-Cryst. Solids **368**, 17 (2013).
[45] M. A. Eastman, P. J. Grandinetti, Y. K. Lee, and A. Pines, J. Magn. Reson. **98**, 333 (1992).

[46]J. L. Markley, W. J. Horsley, and M. P. Klein, J. Chem. Phys. **55**, 3604 (1971).
[47]W. Blumberg, Phys. Rev. **119**, 79 (1960).
[48]I. Lowe and D. Tse, Phys. Rev. **166**, 279 (1968).
[49]D. Tse and S. Hartmann, Phys. Rev. Lett. **21**, 511 (1968).
[50]J. Bodart, V. Bork, T. Cull, H. Ma, P. Fedders, D. Leopold, and R. Norberg, Phys. Rev. B **54**, 15291 (1996).
[51]PhySy Ltd., RMN, version 1.0, www.physyapps.com, PhySy Ltd., Grandview Heights, OH, 2017.
[52]R. K. Harris, E. D. Becker, S. M. C. De Menezes, P. Grangerd, R. E. Hoffman, and K. W. Zilm, Solid State Nucl. Magn. Reson. **33**, 41 (2008).
[53]A. Azzalini and A. Capitanio, *The Skew-Normal and Related Families*, Institute of Mathematical Statistics Monographs (Cambridge University Press, Cambridge, UK, 2014).
[54]A.-R. Grimmer, Chem. Phys. Lett. **119**, 416 (1985).
[55]G. Engelhardt and D. Michel, *High-Resolution Solid-State NMR of Silicates and Zeolites* (John Wiley & Sons, Chichester, 1987).
[56]A. Bax, N. M. Szeverenyi, and G. E. Maciel, J. Magn. Reson. **55**, 494 (1983).
[57]A. Navrotsky, "Energetics of silicate melts," in *Structure, Dynamics and Properties of Silicate Melts*, Volume 32 of Reviews in Mineralogy, edited by J. F. Stebbins, P. F. McMillan, and D. B. Dingwell (Mineralogical Society of America, Washington, DC, 1995), pp. 121–143.
[58]P. C. Hess, "Thermodynamic mixing properties and the structure of silicate melts," in *Structure, Dynamics and Properties of Silicate Melts*, Volume 32 of Reviews in Mineralogy, edited by J. F. Stebbins, P. F. McMillan, and D. B. Dingwell (Mineralogical Society of America, Washington, DC, 1995), pp. 145–190.
[59]R. Dupree, N. Ford, and D. Holland, Phys. Chem. Glasses **28**, 78 (1987).
[60]S. J. Gurman, J. Non-Cryst. Solids **125**, 151 (1990).
[61]B. Vessal, A. Wright, and A. Hannon, J. Non-Cryst. Solids **196**, 233 (1996).
[62]V. Bykov, A. Osipov, and V. Anfilogov, Phys. Chem. Glasses **41**, 10 (2000).
[63]W. J. Malfait, J. Raman Spectrosc. **40**, 1895 (2009).
[64]H. Maekawa, T. Maekawa, K. Kawamura, and T. Yokokawa, J. Non-Cryst. Solids **127**, 53 (1991).
[65]J. V. Smith and C. S. Blackwell, Nature **303**, 223 (1983).
[66]F. Mauri, A. Pasquarello, B. G. Pfrommer, Y.-G. Yoon, and S. G. Louie, Phys. Rev. B **62**, R4786 (2000).
[67]L. Martel, D. Massiot, and M. Deschamps, J. Non-Cryst. Solids **390**, 37 (2014).
[68]W. J. Malfait, W. E. Halter, Y. Morizet, B. H. Meier, and R. Verel, Geochim. Cosmochim. Acta **71**, 6002 (2007).
[69]R. Araujo, J. Non-Cryst. Solids **55**, 257 (1983).
[70]J. Machacek, O. Gedeon, and M. Liska, J. Non-Cryst. Solids **352**, 2173 (2006).
[71]S. Sen and R. Youngman, J. Non-Cryst. Solids **331**, 100 (2003).
[72]A.-R. Grimmer, E. F. Gechner, and G. Molgedey, Chem. Phys. Lett. **77**, 331 (1981).
[73]G. L. Turner, K. A. Smith, R. Kirkpatrick, and E. Oldfieldt, J. Magn. Reson. **70**, 408 (1986).
[74]R. K. Brow, C. C. Phifer, G. L. Turner, and R. J. Kirkpatrick, J. Am. Ceram. Soc. **74**, 1287 (1991).
[75]L. Pauling, *The Nature of the Chemical Bond* (Cornell University Press, Ithaca, NY, 1960).
[76]A. Osipov, L. Osipova, and R. Zainullina, Int. J. Spectrosc. **2015**, 1.
[77]C. O'Shaughnessy, G. S. Henderson, H. W. Nesbitt, G. M. Bancroft, and D. R. Neuville, Chem. Geol. **461**, 82 (2017).

Supplementary Material: Cluster Formation of Network-Modifier Cations in Cesium Silicate Glasses

Daniel Jardón-Álvarez,[1] Kevin J. Sanders,[2] Pyae Phyo,[3] Jay H. Baltisberger,[3] and Philip J. Grandinetti[1]

[1)]*Department of Chemistry, Ohio State University, 100 West 18th Avenue, Columbus, OH 43210, USA*

[2)]*Institut des Sciences Analytiques (CNRS UMR 5280, ENS de Lyon, UCB Lyon 1), Université de Lyon, 5 rue de la Doua, 69100 Villeurbanne, France*

[3)]*Division of Natural Science, Mathematics, and Nursing, Berea College, Berea, Kentucky 40403, USA*

Nominal		Melt	Corrected	
x	w	Temp.	x	w
0.14	6.00	1400 °C	0.067 ± 0.006	13.9 ± 1.2
0.17	5.00	1200 °C	0.113 ± 0.004	7.8 ± 0.3
0.18	4.50	1300 °C	0.175 ± 0.002	4.72 ± 0.04
0.20	4.00	1200 °C	0.179 ± 0.003	4.61 ± 0.06
0.22	3.50	1200 °C	0.218 ± 0.003	3.58 ± 0.06
0.25	3.00	1200 °C	0.234 ± 0.003	3.27 ± 0.05
0.29	2.50	1100 °C	0.263 ± 0.003	2.80 ± 0.05
0.33	2.00	1200 °C	0.298 ± 0.004	2.36 ± 0.04
0.36	1.75	1100 °C	0.31 ± 0.01	2.2 ± 0.1
0.40	1.50	1100 °C	0.36 ± 0.02	1.8 ± 0.1

TABLE S1. Nominal sample compositions, melt temperatures, and NMR corrected compositions of alkali silicate glasses used in this study.

x	T_1/s	β	χ^2_ν	$T_{75\%}$/s
0.067	3.8 ± 0.4	0.52 ± 0.05	1.5	7.1
0.113	4.9 ± 0.4	0.53 ± 0.04	1.5	9.0
0.175	3.7 ± 0.1	0.48 ± 0.01	1.5	7.2
0.179	6.9 ± 0.3	0.51 ± 0.02	1.5	13.0
0.218	6.3 ± 0.6	0.47 ± 0.03	1.3	12.6
0.234	6.3 ± 0.5	0.46 ± 0.02	1.2	12.9
0.263	5.3 ± 0.7	0.59 ± 0.07	2.0	9.1
0.298	4.5 ± 0.4	0.47 ± 0.03	1.6	8.9
0.31	4.4 ± 0.5	0.55 ± 0.05	1.8	7.9
0.36	2.2 ± 0.1	0.46 ± 0.03	1.6	4.4

TABLE S2. Best fit parameters from least-squares analysis of saturation recovery experiments to the stretched exponential function of Eq. (4). Parameter uncertainties are given as one standard deviation. Also listed for each composition is the chi-squared reduced, χ^2_ν, for the best fit and $T_{75\%}$, the 75% recovery time. All compositions are doped with approximately 0.5 wt% CuO.

x	θ_1	$\frac{\pi}{2}(\theta_1)$	τ_m	$\frac{\pi}{2}(\theta_2)$	$n_{t_1} \times n_{t_2}^{(k)}$	Δt_1	Δt_2	$t_2^{(0)}$	$t_2^{(k)}$	n_{ETA}	scans	τ_{rd}	τ_{tot}
0.067	87.1°	8.0 μs	183 ms	5.8 μs	124×600	50.0 μs	12.6 μs	3.8 ms	7.6 ms	50	512	7 s	123 h
0.113	90.0°	7.0 μs	183 ms	5.0 μs	90×600	50.0 μs	12.6 μs	3.8 ms	7.6 ms	40	256	10 s	64 h
0.175	87.1°	6.8 μs	183 ms	4.4 μs	64×600	50.0 μs	12.6 μs	3.8 ms	7.6 ms	40	512	9 s	82 h
0.179	90.0°	7.0 μs	183 ms	5.0 μs	80×600	50.0 μs	12.6 μs	3.8 ms	7.6 ms	40	512	14 s	159 h
0.218	90.0°	6.8 μs	183 ms	4.7 μs	78×600	50.0 μs	12.6 μs	3.8 ms	7.6 ms	40	512	13 s	144 h
0.234	90.0°	6.8 μs	183 ms	4.7 μs	78×600	50.0 μs	12.6 μs	3.8 ms	7.6 ms	40	512	13 s	144 h
0.263	90.0°	6.8 μs	183 ms	4.7 μs	90×600	50.0 μs	12.6 μs	3.8 ms	7.6 ms	40	512	10 s	128 h
0.298	87.1°	6.8 μs	303 ms	4.4 μs	48×600	50.0 μs	12.6 μs	3.8 ms	7.6 ms	40	512	10 s	68 h
0.31	90.0°	6.7 μs	183 ms	4.8 μs	128×128	30.0 μs	50.0 μs	3.2 ms	6.5 ms	100	768	9 s	246 h
0.36	87.1°	8.0 μs	183 ms	5.8 μs	104×600	50.0 μs	12.6 μs	3.8 ms	7.7 ms	100	512	5 s	74 h

TABLE S3. Acquisition parameters used in the shifted echo magic-angle flipping pulse sequence with echo train acquisition[?] . Here, n_{ETA} is the number of echoes acquired during echo train acquisition, τ_{rd} is the recycle delay, and τ_{tot} is the total experiment time. The initial t_1 value was 0.1 μs for all compositions except for $Cs_2O{\cdot}1.9\ SiO_2$, $Cs_2O{\cdot}4.64\ SiO_2$, $Cs_2O{\cdot}7.89\ SiO_2$ which has t_1 of 0.3 μs.

		Q^4							
x	χ^2_ν	y_4/%	ξ_{iso}/ppm	Δ_{iso}/ppm	α_{iso}	$\overline{\delta}_{\mathrm{iso}}$/ppm	s_{iso}/ppm	$\gamma_{1,\mathrm{iso}}$	$\gamma_{2,\mathrm{iso}}$
0.067	1.75	85.6 ± 1.2	-109.95 ± 0.07	4.8 ± 0.1	0.50 ± 0.03	-108.2 ± 0.3	4.5 ± 0.1	0.023 ± 0.002	0.00 ± 0.00
0.113	1.39	74.4 ± 1.0	-109.89 ± 0.07	5.3 ± 0.1	0.75 ± 0.03	-107.4 ± 0.4	4.6 ± 0.1	0.070 ± 0.003	0.02 ± 0.01
0.175	1.72	57.7 ± 0.4	-109.2 ± 0.3	6.9 ± 0.2	1.45 ± 0.06	-104.7 ± 0.8	5.2 ± 0.2	0.28 ± 0.02	0.16 ± 0.02
0.179	2.91	56.5 ± 0.9	-109.4 ± 0.7	6.1 ± 0.4	0.75 ± 0.06	-106.5 ± 0.9	5.3 ± 0.4	0.069 ± 0.009	0.02 ± 0.01
0.218	1.49	44.1 ± 0.8	-108.3 ± 0.7	7.1 ± 0.5	1.3 ± 0.2	-103.8 ± 1.6	5.5 ± 0.8	0.23 ± 0.04	0.12 ± 0.04
0.234	1.61	38.8 ± 0.7	-107.8 ± 0.7	7.7 ± 0.5	1.3 ± 0.2	-102.9 ± 1.7	6.0 ± 0.8	0.23 ± 0.04	0.12 ± 0.03
0.263	1.39	28.6 ± 0.7	-105.9 ± 0.7	8.1 ± 0.7	1.1 ± 0.1	-101.1 ± 1.4	6.5 ± 0.7	0.17 ± 0.02	0.08 ± 0.01
0.298	2.64	15.1 ± 0.6	-103.9 ± 0.7	8.5 ± 0.5	1.2 ± 0.1	-98.7 ± 1.4	6.6 ± 0.6	0.21 ± 0.01	0.11 ± 0.01
0.31	4.02	13.5 ± 0.7	-96.9 ± 0.8	8.5 ± 0.5	0.3 ± 0.1	-95.0 ± 1.1	8.3 ± 0.5	0.009 ± 0.002	0.00 ± 0.00
0.36	1.49	0.7 ± 0.8	-95.5 ± 0.7	8.8 ± 0.7	1.5 ± 0.2	-89.7 ± 1.9	6.6 ± 1.0	0.31 ± 0.3	0.17 ± 0.02

TABLE S4. Best fit parameters area, y_4, location, ξ_{iso}, width, Δ_{iso} and shape α_{iso} as well as calculated standard deviation, s_{iso}, mean chemical shift, $\overline{\delta}_{\mathrm{iso}}$, skewness, $\gamma_{1,\mathrm{iso}}$, and excess kurtosis, $\gamma_{2,\mathrm{iso}}$, for the isotropic dimension for Q^4 sites obtained from the least-squares analysis of 2D MAF spectra in Figs. 1, 2, and 3. Parameter uncertainties are given as 2.58 times one standard deviation (99% confidence limit).

		Q^{3A}			Q^{3B}			Q^{2}		
x	χ^2_ν	y_3/%	$\overline{\delta}_{iso}$/ppm	s_{iso}/ppm	y_3/%	$\overline{\delta}_{iso}$/ppm	s_{iso}/ppm	y_2/%	$\overline{\delta}_{iso}$/ppm	s_{iso}/ppm
0.067	1.75	14.4 ± 1.2	-98.8 ± 1.0	3.2 ± 1.0	-	-	-	-	-	-
0.113	1.39	25.6 ± 1.0	-98.8 ± 0.6	3.6 ± 0.5	-	-	-	-	-	-
0.175	1.72	42.3 ± 0.4	-96.1 ± 0.7	4.0 ± 0.2	-	-	-	-	-	-
0.179	2.91	43.5 ± 0.7	-97.2 ± 0.7	4.6 ± 0.5	-	-	-	-	-	-
0.218	1.49	29.0 ± 0.8	-96.6 ± 0.6	3.9 ± 0.5	26.9 ± 0.8	-95.6 ± 0.7	4.5 ± 0.2	-	-	-
0.234	1.61	21.5 ± 0.7	-96.0 ± 0.7	3.8 ± 0.7	39.7 ± 0.7	-95.2 ± 0.9	5.1 ± 0.2	-	-	-
0.263	1.39	30.9 ± 0.8	-95.8 ± 0.7	4.0 ± 0.8	40.6 ± 0.9	-93.1 ± 0.7	5.5 ± 0.2	-	-	-
0.298	2.64	17.8 ± 0.8	-91.9 ± 0.7	4.5 ± 0.7	67.1 ± 0.8	-92.0 ± 0.7	5.0 ± 0.1	-	-	-
0.31	4.02	-	-	-	81.8 ± 0.9	-92.4 ± 0.7	5.2 ± 0.2	4.7 ± 0.8	-88.7 ± 0.7	2.5 ± 0.4
0.36	1.49	-	-	-	86.5 ± 3.1	-89.0 ± 0.7	4.6 ± 0.7	12.9 ± 3.1	-82.1 ± 0.7	3.0 ± 0.2

TABLE S5. Best fit parameters area, y_n, mean chemical shift $\overline{\delta}_{iso}$, standard deviation s_{iso}, of the Gaussian line shape in the isotropic dimension for each Q^n site obtained from the least-squares analysis of 2D MAF spectra in Figs. 1, 2, and 3. Parameter uncertainties are given as 2.58 times one standard deviation (99% confidence limit).

	Q^4		Q^{3A}	Q^{3B}	Q^2	
x	Δ_0/ppm	m_Δ	ζ_σ/ppm	ζ_σ/ppm	ζ_σ/ppm	η_σ
0.067	4.33 ± 0.06	0.029	89.2 ± 4.1	-	-	-
0.113	4.19 ± 0.03	0.032	87.6 ± 2.1	-	-	-
0.175	4.28 ± 0.03	0.040	89.0 ± 0.6	-	-	-
0.179	4.60 ± 0.06	0.042	91.6 ± 2.6	-	-	-
0.218	4.15 ± 0.07	0.052	84.9 ± 2.3	66.1 ± 2.8	-	-
0.234	4.23 ± 0.09	0.058	84.7 ± 1.1	62.2 ± 2.3	-	-
0.263	4.3 ± 0.1	0.070	83.6 ± 1.2	67.6 ± 1.8	-	-
0.298	4.1 ± 0.1	0.088	79.9 ± 0.9	74.1 ± 4.1	-	-
0.31	4.3 ± 0.2	0.093	-	70.1 ± 0.9	84.7 ± 9.1	0.50 ± 0.02
0.36	4.9 ± 0.2	0.113	-	73.0 ± 1.6	93.5 ± 2.8	0.40 ± 0.02

TABLE S6. Best fit parameters for the nuclear shielding anisotropy parameters, ζ_σ and η_σ for each Q^n obtained from least-squares analysis 2D MAF spectra in Fig. 1, 2, and 3. The value of η_σ was constrained to a value of zero for Q^3 resonances. The standard deviation of gaussian line broadening is held constant at 7.8 ppm for Q^3 and Q^2 resonances. The parameter uncertainties are given as 2.58 times one standard deviation (99% confidence limit).

Q^4							
Site	$A_4(r)$	$\overline{\delta}_{\mathrm{iso}}$/ppm	s_{iso}/ppm	Site	$A_3(r)$	$\overline{\delta}_{\mathrm{iso}}$/ppm	s_{iso}/ppm
$Q^{4,4444}$	$y_4\pi_4^4$	-109.1 ± 0.1	4.2 ± 0.1	$Q^{3,444}$	$y_3\pi_4^3$	-99.3 ± 0.1	2.9 ± 0.1
$Q^{4,4443}$	$y_4 4\pi_4^3\pi_3$	-107.1 ± 0.1	4.4 ± 0.1	$Q^{3,443}$	$y_3 3\pi_4^2\pi_3$	-97.5 ± 0.1	4.2 ± 0.1
$Q^{4,4433}$	$y_4 6\pi_4^2\pi_3^2$	-104.2 ± 0.1	4.2 ± 0.1	$Q^{3,433}$	$y_3 3\pi_4\pi_3^2$	-94.7 ± 0.1	3.1 ± 0.1
$Q^{4,4333}$	$y_4 4\pi_4\pi_3^3$	-99.0 ± 0.2	4.7 ± 0.1	$Q^{3,333}$	$y_3\pi_3^3$	-89.2 ± 0.1	3.6 ± 0.1
$Q^{4,3333}$	$y_4\pi_3^4$	-95.5 ± 0.2	7.3 ± 0.2	-	-	-	-

TABLE S7. Best fit parameters mean chemical shift, $\overline{\delta}_{\mathrm{iso}}$ and standard deviation s_{iso}, for the isotropic dimension for Q^4 and sites obtained from the least-squares analysis of the skew-normal distributions given in Tables S4 and S5 following the RCM using five and four possible Q^4 and Q^3 sites according to the nature of the nearest neighbors. Parameter uncertainties are given as 99% confidence bounds.